Polarization parameters and angular distributions in $\pi^{\pm}p$ elastic scattering at 100 GeV/c and in pp elastic scattering at 100 and 300 GeV/c

R. V. Kline, M. E. Law, and F. M. Pipkin
Harvard University, Cambridge, Massachusetts 02138

I. P. Auer, D. Hill, B. Sandler,* D. Underwood, and A. Yokosawa
Argonne National Laboratory, Argonne, Illinois 60439

A. Jonckheere and P. F. M. Koehler
Fermi National Accelerator Laboratory, Batavia, Illinois 60510

W. Brückner,† O. Chamberlain, G. Shapiro, and H. Steiner
Lawrence Berkeley Laboratory, University of California, Berkeley, California 94720

W. Johnson
Suffolk University, Boston, Massachusetts 02114

J. H. Snyder‡ and M. E. Zeller
Yale University, New Haven, Connecticut 06520

(Received 25 February 1980)

Measurements of the polarization parameters and angular distributions are reported for $\pi^{\pm}p$ elastic scattering at 100 GeV/c and for pp elastic scattering at 100- and 300-GeV/c incident momentum. The $\pi^{\pm}p$ data cover the kinematic range $0.18 \leq -t \leq 1.10$ GeV^2 and are in agreement with current Regge-model predictions. The pp data cover the kinematic range $0.15 \leq -t \leq 1.10$ GeV^2 and $0.15 \leq -t \leq 2.00$ GeV^2 at 100 and 300 GeV/c, respectively, and are found to be consistent with absorption-model predictions.

I. INTRODUCTION

In addition to the searches for totally new phenomena, the higher energies available at Fermilab and the CERN SPS provide the opportunity to test the validity of phenomenological predictions for strong-interaction processes based on low-energy data. A case in point is the measurement of the polarization parameter in elastic scattering. Differential cross sections in elastic scattering at high energies are highly diffractive and thus are well described by analogs to optical phenomena, or by Pomeron exchange in Regge phenomenology. The polarization parameter, arising from an interference between amplitudes, has greater sensitivity to the details of the interaction; in particular, at small scattering angles it reflects the behavior of other t-channel-exchange amplitudes as they interfere with the Pomeron.

Regge-pole models have been formulated which accurately describe πp elastic polarization data up to 45 GeV/c[1]; they predict that the π^+p and the π^-p polarizations will continue to be mirror symmetric, i.e., $P_{\pi^+p}(t) = -P_{\pi^-p}(t)$ for $-t < 1$ GeV^2, and that their magnitudes will decrease with increasing energy approximately as $s^{-1/2}$. These same models, however, are unable to account for the pp elastic polarization data.[2] The usual phenomenology with exchange degeneracy predicts a smoothly varying polarization without zeros for $-t$ less than a few GeV^2, in disagreement with the data throughout the momentum range from 10 to 45 GeV/c. Models which include absorption corrections have been constructed[3-6] and are able to fit adequately the existing data below 100 GeV/c. Their predictions at higher energies must now be tested. Of particular interest is the exploration of the polarization parameter in pp elastic scattering near $t = -1.4$ GeV^2, where the differential cross section develops a dip at incident beam momenta above 100 GeV/c.[7]

The results of this experiment have already been reported in brief communications.[8,9] In this paper we present the details of the experimental method and data reduction, tabulate all of the results, and compare them with the predictions of an absorption model.[3]

II. APPARATUS

Introduction

The need to measure the polarization in the high-$|t|$ region (>1 GeV^2), where the differential cross section is small, placed several constraints on the design of the beam and detector. A beam flux of up to 3×10^7 particles per spill was required, which precluded single-particle detectors being

operated directly in the beam. As a result all information about an event had to be obtained solely from measurements on the scattered particles.

Another consequence of the high incident flux was the potentially high trigger rate due to inelastic events. For this reason the apparatus was designed to provide redundant kinematic information which could be used in the trigger to discriminate against inelastic events.

Beam

The experiment was performed in the $M1$ (East) beam line of the Meson Laboratory at Fermilab. This secondary beam line had a production angle of 3.5 mrad with respect to the primary proton beam. Separation of elastic from quasielastic events, i.e., events originating from protons bound in the nuclei of the target material, depended on knowing the transverse momentum of the beam particle to ±20 MeV/c. This small transverse momentum was achieved by a beam tune at the final focus with very small angular divergence. The parameters of the final beam tunes are listed in Table I.

The discovery of significant polarization in inclusive Λ production[10] led to speculation that our proton beam might also be polarized. Since a secondary proton beam is produced via the parity-conserving strong interaction, the only component of beam polarization which can be nonzero is that normal to the production plane. To first order (i.e., ignoring the 1-mrad downward tilt of the production plane and assuming no net spin precession by the beam-line quadrupoles) this component will be vertical at the polarized target. On the basis of such arguments we installed a system of dipole magnets which eliminated the effect of a nonzero vertical beam polarization by precessing it into the scattering plane. Figure 1 shows the locations and field directions of the magnets which achieved the desired spin precession and restored the beam to its original position and direction at the polarized target.

Polarized proton target

The polarized proton target (PPT) was built at Argonne National Laboratory and has been described elsewhere.[11] The following is a summary of its operating parameters. The target magnet produced a central field of 24.75 kG with a field integral along a diameter of 1130 kG cm. The magnetic field was uniform to ±5 G over the target volume. The target flask was made of teflon and had dimensions 2.0 cm × 2.0 cm transverse to the beam and 8.1 cm along the beam. The target material, ethylene glycol doped with potassium dichromate oxidation products, was deposited into the flask in the form of 2-mm-diameter beads. The resulting volume density of free protons was approximately 0.07 g/cm^3, comparable to that of liquid hydrogen. The target was cooled to an operating temperature of 0.45°K by a closed-loop ^{3}He system in contact with an open ^{4}He system. The target-polarization enhancement was measured once every ten beam spills by digitizing the response to an NMR frequency sweep, while the thermal equilibrium polarization was measured at regular intervals during each running period. Polarizations as high as 90% were achieved although average polarizations for data runs were typically between 75 and 85%. The target enhancement was reversed after every other run, corresponding to a reversal every hour under normal circumstances.

Spectrometer

The scattered particles were detected with the help of a double-arm spectrometer (Fig. 2) built around two superconducting analysis magnets.

TABLE I. Beam parameters.

	Beam momentum (GeV/c)	
	100	300
Momentum bite ($\delta p/p$)	±1%	±1%
Angular divergence at PPT		
horizontal	±0.2 mrad	± <0.1 mrad
vertical	±0.2 mrad	± 0.1 mrad
Beam-spot size at PPT		
horizontal	2.0 cm	1.5 cm
vertical	1.5 cm	1.0 cm
Flux per 1 sec spill	$\leq 1.5 \times 10^7$	$\leq 3 \times 10^7$
Approximate beam composition (π^+:p:K^+)		
primary proton beam energy = 300 GeV	40:54:6%	0:100:0%
primary proton beam energy = 400 GeV	47:47:6%	3: 97:0%

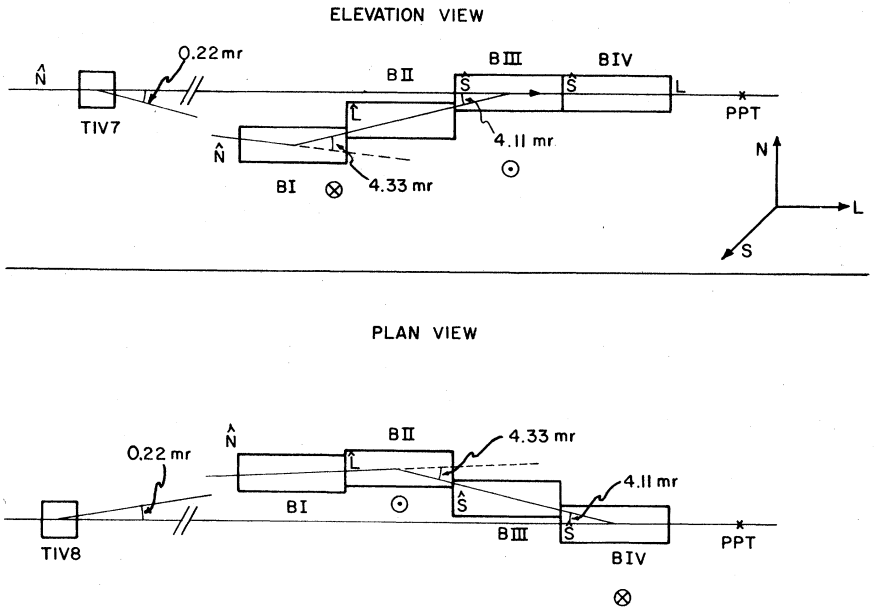

FIG. 1. Arrangement of the spin-precession magnets. At the magnet polarities and bending angles shown, the spin of a beam proton will be precessed from an initial direction $\hat{N}$ (normal to the scattering plane) to direction $\hat{L}$ (along the momentum) and finally to direction $\hat{S}$ (transverse to the beam, in the scattering plane).

Particle trajectories were determined by four pairs of proportional wire chambers (PWC's) on each arm: WS1–WS4 and WR1–WR4 on the "scattered arm" and "recoil arm," respectively. Relevant PWC parameters are listed in Table II. Since the momentum and scattering angle of both final-state particles were determined, the detector, in principle, allowed a four-constraint fit to the hypothesis of elastic scattering for each event.

Four scintillator-tungsten sandwich counters covered the pole faces of the polarized-target magnet to suppress multiparticle final states and events with photons from π° decay or nuclear de-excitation. The halo around the incident beam was rejected by the hole counter H, and a thin counter R indicated the presence of a recoil particle. The locations of these counters are shown in Fig. 3.

In order to keep the beam on its proper course through the spectrometer we equalized the relative counting rates in pairs of "beam-tail" counters which straddled the nominal beam line just upstream of the polarized target and WS2.

Detection efficiencies as calculated by a Monte Carlo simulation are shown in Fig. 4 for three classes of events. The figure depicts the great suppression of nonelastic events relative to elastic events. The principal reasons for this suppression are: the relatively small acceptance of the forward arm for multiparticle final states, the redundancy of kinematic information obtained from the measurements of the recoil and forward scattering angles and the recoil momentum, and the constraint imposed by the momentum determination in the forward arm.

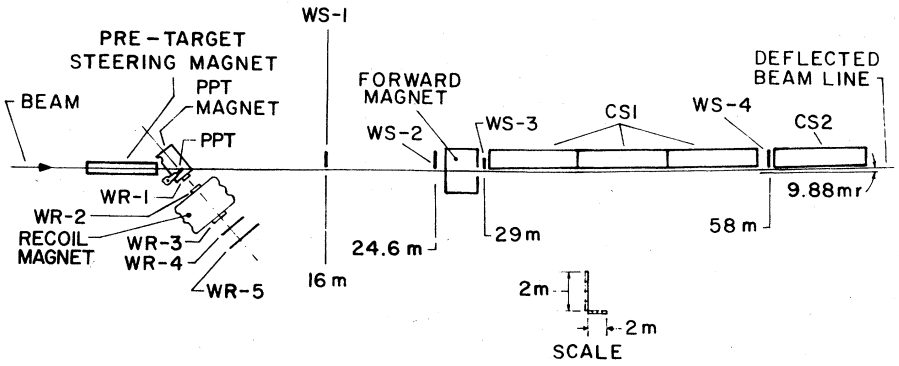

Fig. 2. Plan view of the double-arm spectrometer in the 100-GeV/c geometry.

TABLE II. Summary of proportional-wire-chamber parameters.

PWC	Distance from PPT (cm) 100 GeV/c	300 GeV/c	Wire spacing X (mm)	Y (mm)	Number of wires N_x	N_y
WR1	55		2	2	144	144
WR2	135		2	4	192	88
WR3	325		2	6[a]	245	160
WR4	405		2	6[a]	320	200
WS1	1600	3200	1	1.5	288[b]	128
WS2	2450	4800	1	1.5	408[c]	112
WS3	2950	5300	2	2[a]	192	192
WS4	5900	9500	2	2[a]	312	288

[a]The sense wires in this module were angled at 26° from the horizontal plane to remove ambiguities in track reconstruction in cases of multiple tracks.

[b]The first 48 wires in the WS1X plane were operated at lower voltage than the rest of the chamber to make them insensitive to the unscattered beam.

[c]The first 112 wires in the WS2X plane were operated at lower voltage than the rest of the chamber to make them insensitive to the unscattered beam.

Two threshold Čerenkov counters (CS1, CS2) were placed downstream of the forward-arm analysis magnet to distinguish between scattered pions, kaons, and protons. The counters were made up of 9-m-long sections of 1.2-m-diameter pipe; CS2 consisted of a single section while CS1 consisted of three sections for the 100-GeV/c run and four sections for the 300-GeV/c run. Although the unscattered beam traveled just inside the pipes, thin sheet metal septa prevented its Čerenkov light from reaching the photomultipliers. Both counters were filled with N_2 gas at low pressure, with the temperature and pressure of the gas inside the vessels monitored and automatically maintained at a constant ratio. During the 100-GeV/c run the pressure in CS1 was set just below the kaon threshold (31 Torr) while CS2 was set below the proton threshold (112.6 Torr). Thus, a pion would be identified by large pulse heights in both CS1 and CS2, a kaon by a large pulse height in CS2 and at most a small pulse height in CS1, and a proton by at most small pulse heights in both counters. Since the number of photoelectrons expected in CS2 from a kaon is small, some kaons may have been misidentified as protons; this is not a serious problem because of the small K/p ratio in the beam. On the other hand, protons may have

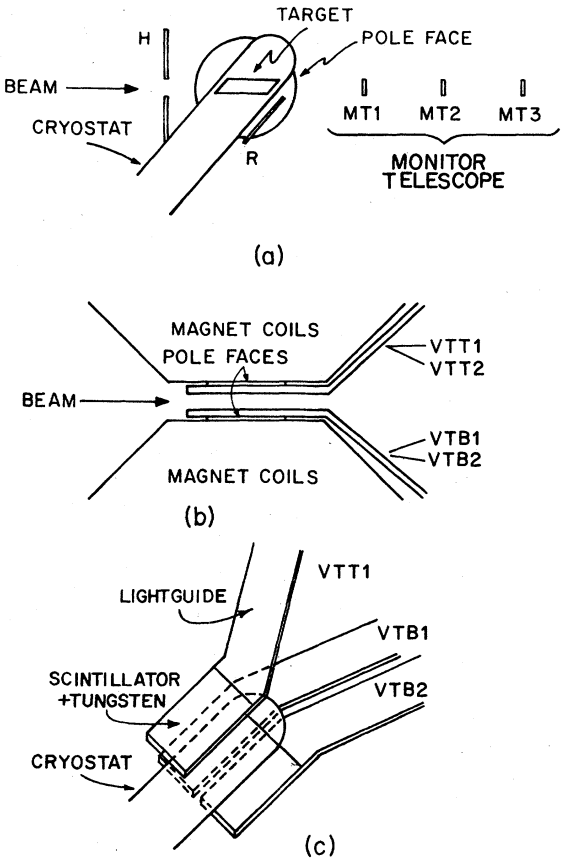

FIG. 3. Arrangement of scintillation counters near the polarized proton target (not drawn to scale).

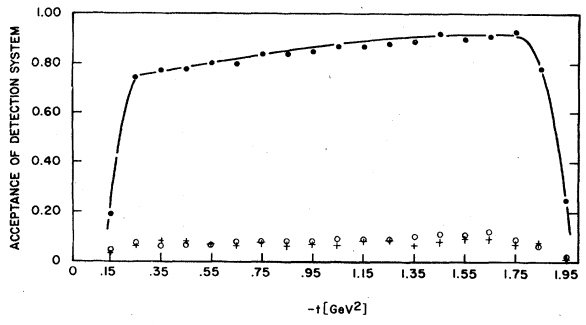

FIG. 4. Monte Carlo–generated t dependence of the detection efficiency for elastic (solid points), quasi-elastic (open points), and inelastic events (crosses).

contaminated the kaon sample by knock-on collisions with the gas in the counters. We estimate about 5% of the protons to be misidentified as kaons, which made it impossible to extract K^+p polarizations from this experiment. During the 300-GeV/c run the pressure in both counters was set above the pion threshold (~10 Torr).

The efficiencies of the Čerenkov counters were measured at 100 GeV/c by reducing the beam intensity and tagging beam particles with a differential Čerenkov counter located upstream of our apparatus; allowing for differences in the scattering cross sections and for decays upstream of CS1 one can calculate the efficiencies directly. The pion efficiency of CS1 was found to be 99.3%. The pion efficiency of CS2 was determined by looking at its pulse-height spectrum for events for which CS1 registered a large pulse height, i.e., a nearly pure pion sample. Such a plot is given in Fig. 5. The lowest channel contains approximately 2% of the events, corresponding to a CS2 efficiency for pions of 98%.

At 300 GeV/c, with protons comprising 97% or more of the beam, contamination of protons by pions was important only at high $|t|$; even at $t = -1.3$ GeV^2, proton events should be about three times more numerous than pion events. Using the differential Čerenkov counter we found the pion inefficiency of CS1 to be about 5%, sufficiently small to ensure a clean pp polarization measurement even at high $|t|$.

Logic

The fast-trigger logic was uniquely adapted to this experiment in two respects. First, to minimize delay times due to the length of the forward arm, the trigger underwent several levels of refinement at spatially dispersed logic stations; at the first unsatisfied coincidence requirement the dead-time gates were automatically reset and the system reactivated. The dead time was less than 2 μs for any reaction which satisfied the first coincidence requirement (the presence of a recoiling particle) but failed to interrupt the on-line computer. In the majority (>90%) of the reactions the apparatus reset within 200 ns. Dead times resulting from the fast logic were less than 5% of the live time at the highest fluxes. Second, the correlation between momenta and trajectories of final-state particles in elastic scattering made it possible to enhance the trigger for desired events through the use of two-dimensional matrix coincidence units.

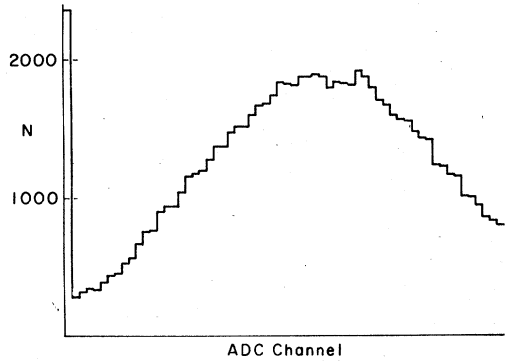

FIG. 5. Pulse-height spectrum of CS2 when gated on a large pulse height in CS1 at a beam momentum of + 100 GeV/c.

The inputs to the row and column elements of these matrices came from groups of wires in appropriate PWC's, with each intersection between row and column elements switchable between an active and an inactive state. If active, an intersection produced a logical TRUE signal if the respective inputs were in time coincidence ($\Delta t \leq 50$ ns). The signals from active intersections were either connected together to form a single OR output for use in standard logic modules, or were grouped such that members of each group represented a common trajectory angle through the respective chambers. These common angle outputs were then used as input signals to the row or column of a subsequent matrix.

The matrices could exploit the following properties exhibited by elastic events:

(a) The trajectories from WR3X to WR4X are nearly parallel, independent of t.

(b) The trajectories of the beam, the forward, and the recoil particle are coplanar.

(c) The forward and recoil scattering angles are well correlated.

(d) The deflection angle in the forward analysis magnet is constant for all practical purposes.

In practice, even at intensities up to $(2-3)\times 10^7$ particles per pulse, it was possible to reduce the trigger rate to manageable levels by requiring a recoil particle to pass through all the recoil-arm chambers in coincidence with a particle in WS1X and no signal in any of the pole-tip veto counters.

Flux monitors

Since the polarization parameter is proportional to the difference of the differential cross sections for the two spin orientations of the polarized target divided by their sum, a precise knowledge of the relative numbers of incident particles for the two target enhancements is needed. Since the beam intensity was too high for scintillators or proportional chambers and too low for ion chambers to work reliably in the beam, this experiment relied on two indirect flux monitors:

(1) A pair of scintillation-counter telescopes, each consisting of three elements, which pointed toward the polarized target from a scattering angle of 100 mrad. These monitors were located at azimuthal angles of 90° and 270° in order to make them insensitive to the polarization of the target. (Only the lower telescope was in place during the 100-GeV/c run). We scaled the threefold coincidences between the elements for the up and down monitor telescope separately, each in anticoincidence with a signal from the hole veto counter in front of the target; they are referred to as $M_{T\cdot\bar{H}(U)}$ and $M_{T\cdot\bar{H}(D)}$.

(2) Two twofold coincidences between diagonally opposite elements of the pole-tip veto counters were recorded:

$$M_{VA} = VTT1\cdot VTB2 \text{ and } M_{VB} = VTT2\cdot VTB1 .$$

The ratios of these four monitors agreed to within a few percent from run to run. $M_{T\cdot\bar{H}(U)}$ and $M_{T\cdot\bar{H}(D)}$ were calibrated in terms of the beam flux by scaling coincidence counts from a pair of crossed scintillation counters which were placed in the beam just upstream of the target. The calibration factor was found to be constant over a wide range of intensities, until the beam counters began to saturate at a flux of 5×10^6 particles per pulse; this factor was used to convert monitor counts to beam fluxes up to the highest intensities.

For the data analysis we formed the following combinations of monitor counts:

$$M_T = M_{T\cdot\bar{H}(U)} + M_{T\cdot\bar{H}(D)} ,$$

$$M_V = M_{VA} + M_{VB} ,$$

and

$$F = M_T + 0.01 M_V .$$

A weight factor of 0.01 was chosen to equalize the counting rates from the two types of monitors.

In many polarized-target experiments, the quasielastic background has been used as the principal monitor. In this experiment, however, the selective acceptance of the apparatus resulted in a final data sample which contained only about half as many quasielastic events as elastic events. Thus, normalizing to the quasielastic background would have meant that the statistical error on the background events would have added significantly to the final uncertainty in the polarization parameters at small $|t|$. Therefore, we used the numbers of quasielastic events only as a check on the other monitors. This was done by calculating the asymmetry in these events with respect to target-spin orientation. This background asymmetry should be zero.

Data acquisition

The on-line computer which monitored the apparatus and recorded the data on magnetic tape was interfaced to the detectors by a conventional CAMAC system. For each event it recorded the position information from the PWC's, pulse heights from the Čerenkov counters, and the contents of several latch modules which tagged the status of a number of scintillation counters. (This last information was not actually used in the analysis.) The scaler data for the monitors and the digitized NMR data for the target polarization were recorded once every beam spill.

When not engaged in the acquisition or recording of data, the on-line computer processed the most recent events to provide diagnostic information on the apparatus. Typical of such information were PWC wire histograms and pulse-height spectra for the Čerenkov counters. A useful feature of the diagnostic program was its ability to make such wire histograms or spectra depend on the presence (or absence) of a signal in a specified PWC. This was particularly helpful in locating failures in the electronics associated with the PWC's.

The data for this experiment were collected during three separate running periods. The first of these was devoted entirely to data taking at 100 GeV/c incident beam momentum. After that, the forward-arm geometry was stretched to the 300-GeV/c configuration for the final two running periods.

III. DATA ANALYSIS

The data-reduction process can be divided into three well-defined stages:

(1) The processing of the raw-data tapes to eliminate those triggers in which it was not possible to reconstruct a track on each arm, the elimination of unnecessary information from acceptable events, and the production of first-pass-analysis magnetic tapes.

(2) The kinematic analysis of the reconstructed events and the production of second-pass magnetic tapes containing kinematic information and event status flags.

(3) The extraction of elastic events and the study of monitor normalizations.

Raw-data-tape processing

In the first stage of the analysis particle tracks in both dimensions were reconstructed from wire-chamber latches. Our criteria for selecting events to be passed from the raw-data tapes to subsequent stages of the analysis were determined by the need to reconstruct the momentum and the azimuthal

and polar scattering angles of each particle. We consider the requirements on each arm separately.

On the forward arm we required latched data in WS1X and either WS2X or WS3X in order to reconstruct the horizontal projected angle. The combination of WS2X and WS3X was unacceptable since those two chambers were too close to allow an accurate measurement of the angle. To reconstruct the vertical projected angle we required WS1Y and any other Y chamber, or else WS2Y and WS4Y. Again, the WS2-WS3 combination was rejected because it yielded too imprecise a determination of the angle. (Note that requiring a 3Y or 4Y chamber on either arm implicitly required that the X coordinate of the particle be known, since on both arms these planes had their wires at an angle of 26° from the horizontal.)

On the recoil arm, the need to reconstruct the momentum accurately led us to require all four X chambers. To reconstruct the vertical projected angle (ascension angle) we required WR2Y and any other recoil Y chamber.

Triggers which satisfied the above conditions contained the necessary information to reconstruct angles and the recoil momentum. However, this information was sufficient only for "clean" events in which each required chamber had only one cluster. Often one or more chambers had multiple clusters; in order to recover events in such cases, while admitting minimal inelastic background, we imposed cuts based on the following arguments. First, we eliminated events with multiple clusters in both the 1X and 2X chambers because there was no unambiguous way to retrieve events with two tracks on either arm. Second, due to the fact that the chambers downstream of the analysis magnets should be relatively clean because these magnets sweep low-momentum particles away from the chambers, we eliminated events with multiple clusters upstream and downstream of an analysis magnet. Our requirements on the vertical projected angles were less stringent because the system had more redundancy in this dimension. The specific cuts imposed on the data are listed in Table III.

TABLE III. Proportional-wire-chamber requirements imposed on reconstructed events. Here "WS1X" means "one or more signals in PWC plane WS1X," "M(WS1X)" means "more than one signal in plane WS1X," and "$\bar{s}$(WS1X)" means "not one and only one signal in plane WS1X," i.e., either zero or more than one. $\oplus$ represents logical OR. $\otimes$ represents logical AND.

Signal requirements
(1) WS1X $\otimes$ (WS2X $\oplus$ WS3X)
(2) WS1Y $\otimes$ (WS2Y $\oplus$ WS3Y $\oplus$ WS4Y) $\oplus$ WS2Y $\otimes$ WS4Y
(3) WR1X $\otimes$ WR2X $\otimes$ WR3X $\otimes$ WR4X
(4) WR2Y $\otimes$ (WR1Y $\oplus$ WR3Y $\oplus$ WR4Y)
Multiplicity requirements eliminate
(1) M(WS1X) $\otimes$ M(WS2X) $\oplus$ M(WR1X) $\otimes$ M(WR2X)
(2) M(WR3X) $\otimes$ M(WR4X)
(3) [M(WS1X) $\oplus$ M(WS2X)] $\otimes$ [$\bar{s}$(WS3X $\oplus$ $\bar{s}$(WS4X)]
(4) $\bar{s}$(WS1Y) $\otimes$ $\bar{s}$(WS2Y) $\otimes$ $\bar{s}$(WS3Y) $\otimes$ $\bar{s}$(WS4Y)
(5) $\bar{s}$(WR1Y) $\otimes$ $\bar{s}$(WR2Y) $\otimes$ $\bar{s}$(WR3Y) $\otimes$ $\bar{s}$(WR4Y)

Kinetic analysis

In the second stage of the analysis we constructed positions and angles from the wire latch data on the first-pass tapes and used these to calculate kinematic variables characterizing each event. Figure 6 defines our coordinate system. We first constructed projected angles ψ_s, ψ_s', ψ_r, and ψ_r' in the x-z plane, ascension angles α_r and α_s, and the horizontal components of the observed momenta as determined by the differences between the appropriate angles ψ' and ψ. Having determined the momentum of the recoil particle in the spectrometer, we corrected for the energy loss suffered by the recoil particle in traversing the

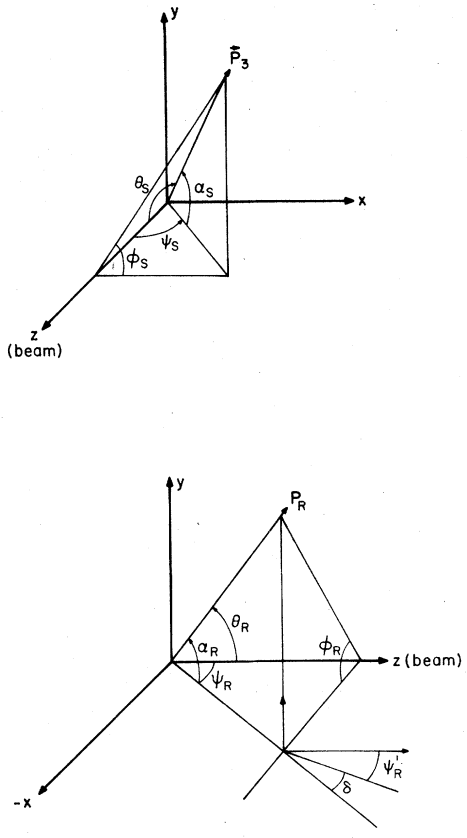

FIG. 6. Definitions of kinematic variables used in the reconstruction of events.

target; the transverse coordinates of the production vertex needed for this correction were obtained by extrapolation of the forward-arm trajectory back to the target. After compensation for the deflections due to the target magnet, laboratory angles θ_s, θ_r, ϕ_s, and ϕ_r were calculated. This gave us six quantities characterizing each event: two scattering angles, two azimuthal angles, and two momenta.

In order to separate the elastic events from the quasielastic background, separate values for t were calculated from each scattering angle and from the recoil momentum, according to the formulas

$$t_1 = 2m_p(m_p - E_r),$$

$$t_2 = \frac{-(2m_p P_B \cos\theta_r)^2}{(m_p + E_B)^2 - (P_B \cos\theta_r)^2},$$

$$t_3 = -P_B{}^2\theta_s{}^2.$$

E_B and P_B are the nominal energy and momentum of the beam particle and E_r is the energy of the recoil proton.

From these an average value t was obtained by minimizing the quantity

$$\chi^2 = \sum_{i=1}^{3} (t - t_i)^2/\delta t_i,$$

where δt_i are uncertainties in the respective values of t_i as calculated for each event from chamber resolution, estimated multiple scattering, and the error on the energy-loss compensation. As a measure of the coplanarity of the final-state particle trajectories and the beam momentum vector, we formed

$$\Delta\phi/\delta\phi \equiv (\phi_s - \phi_r)/(\delta\phi_s{}^2 + \delta\phi_r{}^2)^{1/2}.$$

The quantities t, t_i, δt_i, and $\Delta\phi/\delta\phi$, along with the χ^2, the Čerenkov pulse heights, and a status flag for the event were written on a second-pass magnetic tape. The status flag preserved certain conditions for subsequent data manipulation. In essence, these indicated incorrect track reconstruction, missing chamber data, or inconsistency between momentum or position and the elastic hypothesis.

Extraction of elastic events and polarization parameters

In the final stage of the data-reduction process, the tapes containing kinematic information for each event were used to generate histograms of event distributions in $\chi^2 - \Delta\phi/\delta\phi$ space at the various values of $|t|$. Since no calculations were involved, this step could be repeated easily to study the effects of various cuts on the data. Figure 7 indicates schematically how we defined signal and background regions in χ^2-$\Delta\phi/\delta\phi$ space. From these plots the number of elastic events in each run in a particular kinematic region could be extracted.

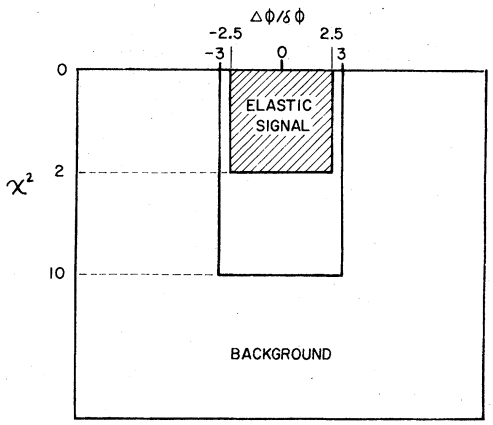

FIG. 7. Definition of elastic signal and background regions in χ^2 and $\Delta\phi/\delta\phi$ space.

Distributions of events versus χ^2 or $\Delta\phi/\delta\phi$, gated by specified limits on the complementary variable, are shown in Figs. 8 and 9. The signal-to-background ratio for pp scattering at 300 GeV/c varied from typically 20:1 for $-t < 0.5$ GeV^2 to a worst case of 0.8:1 at $-t = 1.35$ GeV^2.

As discussed above, the numbers of elastic events for each target polarization had to be normalized to appropriate monitors. To that end an interactive cathode-ray-tube display program was used to investigate the detailed behavior of the

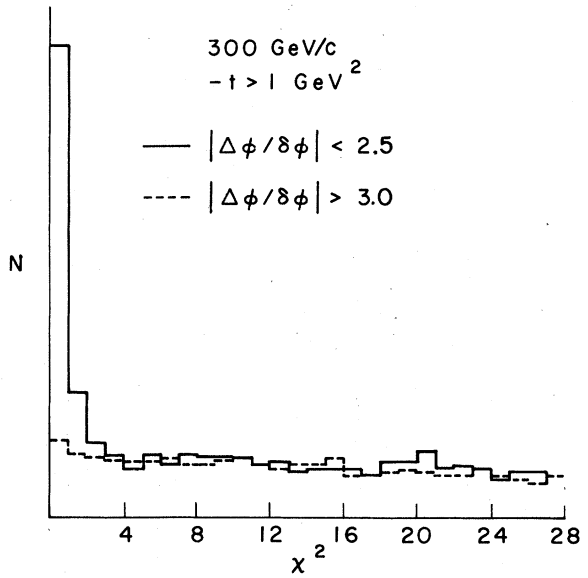

FIG. 8. Histogram of reconstructed coplanar and noncoplanar pp event samples as function of χ^2.

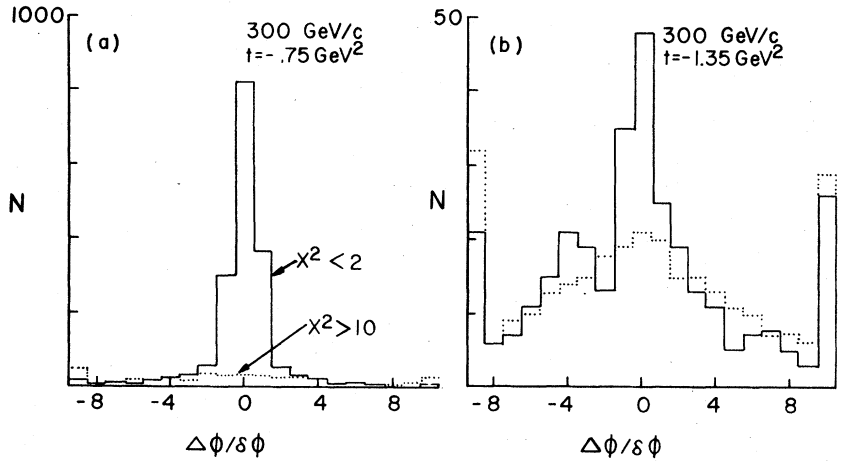

FIG. 9. Histograms of reconstructed elastic and nonelastic pp event samples as function of $\Delta\phi/\delta\phi$; (a) at $t=-0.75$ GeV^2; (b) at $t=-1.35$ GeV^2.

system on a run-by-run basis. Ratios of scalers or data and associated statistical uncertainties were calculated and displayed versus run number in a point plot. Typical of such quantities were ratios of beam monitors and ratios of elastic and background events to such monitors.

In the above study, fluctuations and long-term drifts of these ratios were observed which were larger than could be explained from statistical uncertainties alone. The fluctuations were caused by variations in the overall detection efficiency of the apparatus resulting from pulse-to-pulse differences in the incident beam flux. To prevent these variations from affecting the relevant ratios, we derived effective monitor counts M'_T and M'_V for use in subsequent calculations of these ratios:

$$M'_T=\sum_{i=1}^{n_s} M_{Ti}(1-f_{M_T}M_{Ti})(1-f_{M_V}M_{Vi}),$$

$$M'_V=\sum_{i=1}^{n_s} M_{Vi}(1-f_{M_T}M_{Ti})(1-f_{M_V}M_{Vi}),$$

where M_{Ti} and M_{Vi} are the counts in the two types of flux monitors during beam pulse i, n_s is the number of beam pulses in a data run, and the weight factors f_{M_T} and f_{M_V} were empirically determined.

This correction was not entirely *ad hoc*, even though the precise values of f_{M_T} and f_{M_V} were not calculated theoretically. First, instantaneous flux variations necessarily affected the dead time of the apparatus, and crude calculations resulted in weight factors within a factor of 2 of those used. Second, the weight factors remained nearly constant over the entire set of data runs. Third, the χ^2 value for the fits to a constant ratio of events to monitor counts were rather stable with respect to changes of the weight factors up to 25% of their value but increased rapidly with larger changes. In fact, we chose the weight factors which gave the smallest value of χ^2. The final polarization parameters were also constant, within quoted errors, for changes of up to 25% in these factors.

While this procedure decreased the extent of the run-to-run fluctuations, there still existed long-term drifts which, if ignored, would have led to spurious asymmetries. We dealt with these drifts by dividing the data into sets of runs in which the ratios were consistent, compensated each ratio within a set to remove the drift, and calculated a total uncertainty on the ratio which included both statistical and estimated systematic errors. In this context "consistent" means that each set contained a reasonable number of runs (at least 20), that the run-to-run variations within the set were not much larger than expected from statistical fluctuations, and that a plot of the ratios for the runs within a set versus time of the run was statistically consistent with a straight-line fit, not necessarily of zero slope. The slope calculated in the fit was then used to make a linear correction to the ratios. Note that this process was independent of the orientation of the target polarization. It led to fractional changes in the ratios which were smaller than statistical uncertainties in those ratios for all but the smallest t bins.

In this process we have dealt with the number of elastic events summed over all t bins. The fractional statistical uncertainty on the ratio of total elastic events to monitors, ϵ_{stat}, is thus a t-independent quantity. To calculate uncertainties in the polarization as a function of t it was necessary to calculate the statistical uncertainties for each value of t and to estimate the systematic errors on the ratios which go into the polarization

calculation.

These systematic uncertainties were of several types: First, there are those which affected the overall normalization of the data and therefore had the effect of multiplying the observed polarization by a scale factor. An example of a source of this type is the uncertainty in the target polarization. In our case the combined error ϵ_1 from such sources was 5%. Because our polarization results are not far from zero, this type of error is negligible for this experiment. A second type of systematic error, ϵ_2, has the effect of shifting the zero of the polarization for all points up or down. An example would be systematic fluctuations in the monitoring counters. This type of uncertainty contributed a systematic error of 0.2% for the 100-GeV/c data and 0.5% for the 300-GeV/c data, as described below. Finally, during the course of the experiment we often observed small but statistically significant fluctuations in the ratios of the number of elastic events to various monitors. Because of these fluctuations, whose cause was never completely understood, we scaled up our statistical uncertainties according to the following method.

The overall uncertainty $\epsilon_{\text{tot}}(t)$ associated with a given t bin was assumed to be given by

$$\epsilon_{\text{tot}}(t) = (\epsilon_3^{\,2} + \epsilon_{\text{stat}}^{\,2})^{1/2},$$

where ϵ_3 was assumed to be the same for all values of t and was introduced to make our error estimates more realistic. To evaluate ϵ_3, we first defined ϵ^*_{stat} to be the statistical uncertainty of the ratio of the number of all elastic events (i.e., summed over t) to monitor. The systematic error ϵ_3 was taken to be that quantity which, when added in quadrature with ϵ^*_{stat}, resulted in $\chi^2/N_f = 1$ for the straight-line fit; i.e., if (χ^2/N_f) is the value calculated from the fit, if the errors are assumed to be purely statistical, then

$$\epsilon_3 = \left[\left(\frac{\chi^2}{N_f}\right)_0 - 1\right]^{1/2} \epsilon^*_{\text{stat}}.$$

The contribution of this systematic error to the total uncertainty of the polarization results was typically less than 0.5% and thus was negligible at all but the smallest $|t|$ values. Strictly speaking, this systematic error (for example, the error caused by rate-dependent effects) could be more t-dependent than our procedure would indicate. However, since the numbers of events are so heavily dominated by the first few bins at small $|t|$, we did not do a bin-by-bin error analysis.

The procedure outlined above was followed for all of the 100-GeV/c data and for the 300-GeV/c data in the second run. During the third run (300-GeV/c data) the apparatus was not triggered on low-$|t|$ events; since the uncertainties were dominated by statistical uncertainties, we simply normalized to background.

Polarizations were calculated according to the formula

$$P(t) = \frac{\sum N_+/\sum F'_+ - \sum N_-/\sum F'_-}{P_T^-(\sum N_+^{\text{el}}/\sum F'_+) + P_T^+(\sum N_-^{\text{el}}/\sum F'_-)},$$

where + (−) refers to the direction of the target polarization being normal (antinormal) to the scattering plane, N refers to all of the events within the central χ^2-$\Delta\phi/\delta\phi$ region, N^{el} refers to the elastic events in this region, P_T is the average target polarization (weighted by monitor counts), $F' = M'_T + 0.01\, M'_V$ is the combined rate-corrected flux monitor, and the summations are taken over all runs. We calculated a total uncertainty in the ratio of elastic events to monitors as described above and a total uncertainty in the polarization

$$\delta P(t) = \frac{1}{P_T} \frac{\sum (N_+ + N_-)}{\sum (N_+^{\text{el}} + N_-^{\text{el}})} \epsilon_{\text{tot}}(t).$$

The sources and relative sizes of the errors contributing to the total calculated error are summarized in Table IV.

As a check on the normalization the same procedure was applied to the background events. These should be unpolarized because they are dominated by scattering from bound, unpolarized nucleons. Figure 10 shows that all background asymmetries were consistent with zero except in the set of pp data at 300 GeV/c which, when normalized to monitors, had a statistically significant nonzero value of 0.005 ± 0.002 when averaged over all t. We were unable to account for this background asymmetry in any reasonable way and assigned an additive systematic uncertainty of 0.005 to our pp polarizations at 300 GeV/c, i.e., we allowed the zero on the polarization scale to shift up or down by 0.005.

An independent analysis, with different cuts and procedures, was carried out on part of the data. The results obtained were in substantial agreement with those of the analysis presented here.

IV. RESULTS AND MODEL COMPARISONS

πp scattering

Tables V and VI list our results for the angular distributions and polarization parameters in $\pi^+ p$ and $\pi^- p$ elastic scattering at 100 GeV/c. Instead of determining an absolute normalization for our angular distributions we normalized them at $t = -0.55$ GeV^2 to the differential cross-section values measured by Akerlof *et al.*[7] The results for $\pi^+ p$ and $\pi^- p$ are shown in Fig. 11. Our data agree

TABLE IV. Sources and sizes of errors quoted for the polarization results.

Source of error	Type of error	Typical size of error
Statistical uncertainty	Statistical, adds in quadrature	0.20% at $t=-0.2$ GeV^2 10% at $t=-1.2$ GeV^2
Systematic fluctuations	Systematic, adds in quadrature	0.50% at all t
Uncertainty in target polarization	Systematic, multiplies scale	5% at all t
Difference between monitor and background normalizations	Systematic, adds linearly to scale	<0.20% at all t (0.50% for pp scattering at 300 GeV/c)

with those of Akerlof *et al.*[7] over the full t range.

Our results for the π^+p and π^-p polarization parameters are shown in Fig. 12. For $-t<0.6$ GeV^2 our data still exhibit the mirror symmetry $P_{\pi^+p}(t)$ $= -P_{\pi^-p}(t)$ which has been observed at lower momenta.[12,13] The curves in Fig. 12 represent the polarization parameters which were measured at 10 GeV/c (Ref. 13) and scaled up to 100 GeV/c according to $s^{\alpha(t)}$, with the assumption of Pomeron and ρ exchange prescribing $\alpha(t)=-0.5+0.9t$. The agreement between the curves and our data for $-t<0.6$ GeV^2 shows that the energy dependence of the πp polarization parameters is consistent with predicted Regge behavior.

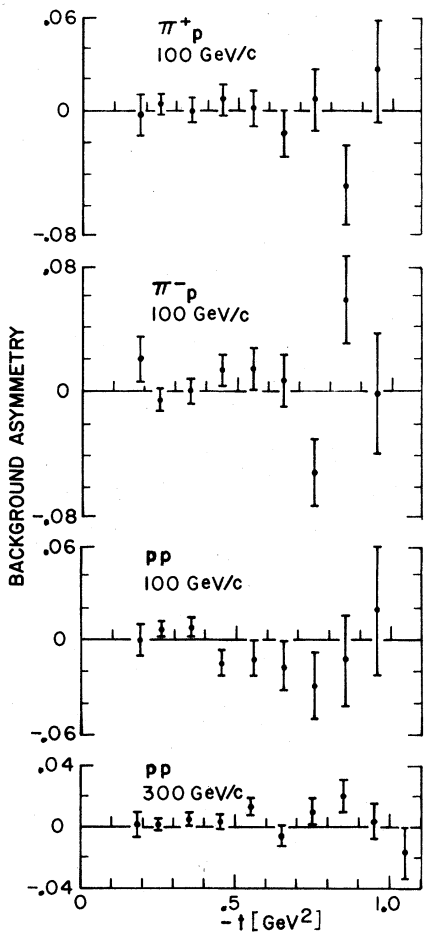

FIG. 10. Asymmetry of the background events when using monitor normalization for π^+p and π^-p scattering at 100 GeV/c and for pp scattering at 100 and 300 GeV/c.

Since the πp polarization is approximately given by[3]

$$P(\pi^\pm p)=(\mathrm{Im}N_0)[\mathrm{Re}(F_0\pm F_1)]\,,$$

where N and F denote helicity nonflip and flip amplitudes, respectively, and where the subscripts indicate isospin, our polarization data can be used to place a limit on the isosinglet helicity-flip contribution, i.e., f exchange and, in some models,

TABLE V. Angular distributions for π^+p and π^-p elastic scattering at 100 GeV/c.

	π^+p		π^-p	
$-t$ (GeV^2)	$N(t)$	$\delta N(t)$	$N(t)$	$\delta N(t)$
0.18	178 879	1074	142 653	895
0.25	151 062	505	120 704	455
0.35	73 260	339	58 557	305
0.45	36 405	236	28 284	209
0.55	18 283	164	14 373	147
0.65	8 949	115	6 937	101
0.75	4 271	80	3 487	67
0.85	2 400	58	1 688	47
0.95	1 327	42	948	35
1.05	666	30	446	24
1.15	339	22	227	18
1.25	231	18	135	13
1.35	128	13.5	102	11
1.45	65	9.7	27.5	7.9
1.55	29.5	7.5	16.4	4.9
1.65	32.4	6.1	8.7	10.3
1.75	12.0	3.6	2.2	9.4

TABLE VI. Polarization parameters for π^+p and π^-p elastic scattering at 100 GeV/c.

	π^+p		π^-p	
$-t$ (GeV^2)	$P(t)$	$\delta P(t)$	$P(t)$	$\delta P(t)$
0.18–0.20	0.037	0.007	−0.023	0.008
0.20–0.30	0.025	0.004	−0.028	0.004
0.30–0.40	0.009	0.005	−0.024	0.006
0.40–0.50	0.003	0.007	−0.001	0.008
0.50–0.60	−0.009	0.010	−0.014	0.011
0.60–0.70	0.005	0.014	−0.029	0.016
0.70–0.80	−0.001	0.020	−0.018	0.023
0.80–0.90	−0.004	0.027	0.001	0.032
0.90–1.00	−0.016	0.036	0.008	0.043
1.00–1.10	−0.035	0.050	−0.025	0.061
1.10–1.20	−0.077	0.070	0.018	0.084
1.20–1.30	−0.097	0.085	−0.082	0.111
1.30–1.40	0.012	0.112	−0.007	0.129

an additional "diffractive" contribution. Our results are found to be consistent with Regge behavior for F_0, in agreement with polarization data at momenta up to 20 GeV/c. We do not find any evidence to support the tentative identification of non-Regge F_0 behavior in the Serpukhov data.[14,15]

In order to test the ability of Regge phenomenology to account for our data, we selected from among the many models of strong-interaction physics the model of Kane and Seidl.[3] This model appealed to us for several reasons. First, the authors have attempted to describe, in a unified fashion, all of the high-energy two-body hadron physics in which the nuclear force is generated through meson exchange; variations in the parametrization of the model from reaction to reaction were introduced only when dictated by the underlying physics. Second, this model is closely connected to Regge-pole phenomenology and is not simply a fit of some complicated function or functions to published data. Third, it correlates an immense amount of disparate experimental data, much of which is not easily described by pure pole models. Finally, the model is explicitly described in the literature. A summary of the model's technical features is given in the Appendix, together with a collection of the formulas needed to calculate amplitudes and observables.

Figure 13 shows resulting fits to $\pi^\pm p$ polarization data below 100 GeV/c, and Fig. 14 compares the predictions at 100 GeV/c and the results of this experiment. The agreement is very good. An interesting prediction of the model, and one which could be directly tested with new high-intensity pion beams, is the existence of a dip in the differential cross section for πp elastic scattering near $t = -2.3$ GeV^2, accompanied by a change in

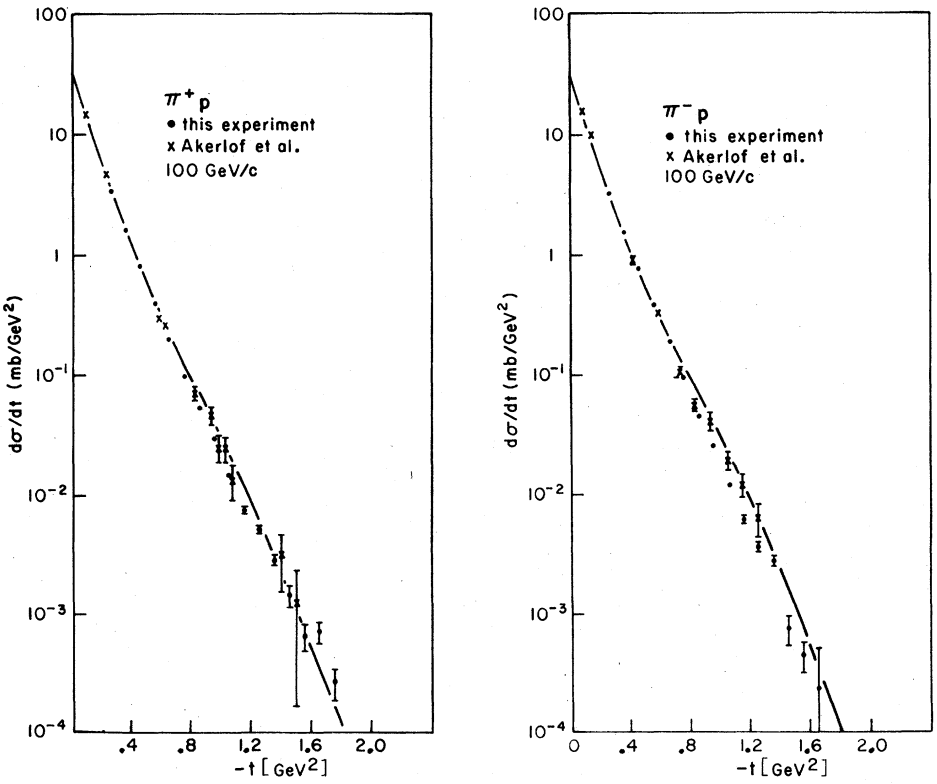

FIG. 11. Differential cross sections for $\pi^\pm p$ elastic scattering at 100 GeV/c.

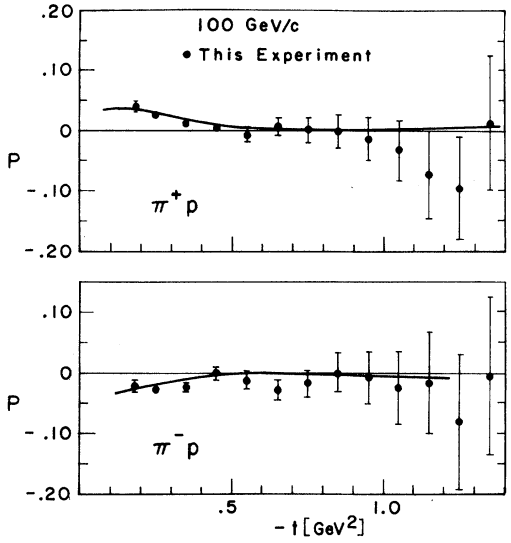

FIG. 12. Polarization parameters for $\pi^+ p$ and $\pi^- p$ elastic scattering at 100 GeV/c from this experiment. The solid curves represent the t dependence of the corresponding data measured at 10 GeV/c after scaling to 100 GeV/c as described in the text.

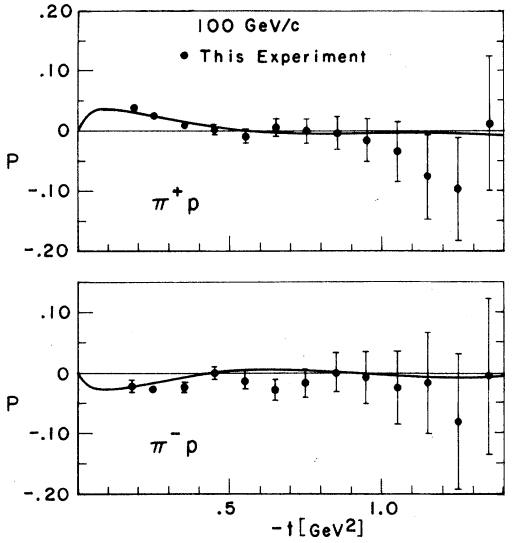

FIG. 14. Comparison between the predictions of the Kane and Seidl model for the $\pi^\pm p$ polarization parameters at 100 GeV/c and the results from this experiment.

the polarization from −0.50 to +0.75. This structure arises from a nearby diffraction zero and is analogous to the dip in the pp differential cross section at $t = -1.4$ GeV^2.

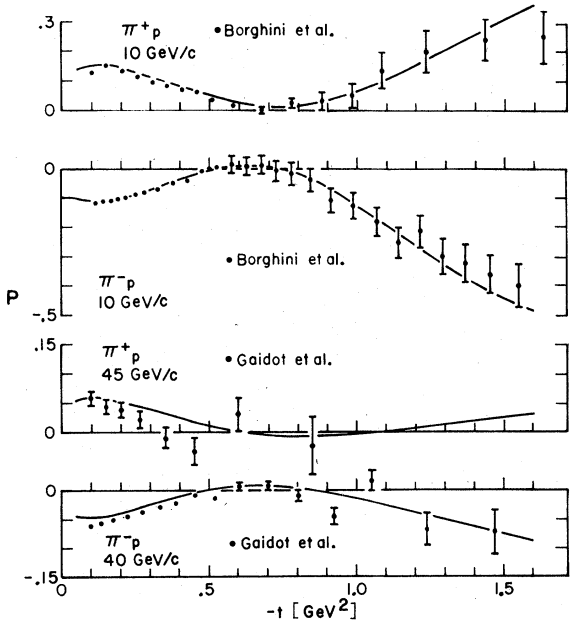

FIG. 13. Fits of the Kane and Seidl model to $\pi^\pm p$ polarization data at 10 and near 40 GeV/c.

pp scattering

Tables VII and VIII list our results for the angular distributions and polarization parameters in pp elastic scattering at 100 and 300 GeV/c. In order to make a comparison with previously reported differential-cross-section data at corresponding momenta obtained at Fermilab[7] and at the CERN ISR,[16] we normalized our angular distributions to these data at $t = -0.55$ GeV^2. At both momenta the agreement is very good over the entire t range, as can be seen in Fig. 15.

Our results for the pp polarization parameters at 100 and 300 GeV/c are shown in Fig. 16, together with data points obtained by Corcoran *et al.*[17] at 110 GeV/c. Since pure pole-model predictions have been unsuccessful in accounting for pp polarization data even at low momenta, extrapolations of the pp polarization behavior from low-energy data to 100 and 300 GeV/c are quite unreliable. Consequently, we first discuss our results in the context of existing lower-energy data in order to identify trends in the structure of the polarization parameters as the energy increases. Then we compare our results with predictions of the model by Kane and Seidl.[3]

Figure 17 shows a selection of pp polarization data at 6, 10, 14, 17.5, 24, and 45 GeV/c incident laboratory momentum.[12,15,18,19] At 6 GeV/c there exists a dip near $t = -0.8$ GeV^2 which has changed to a double zero by 10 GeV/c. This structure persists through 17.5 GeV/c and may still be present at 24 GeV/c. However, the polarization data at

TABLE VII. Angular distributions for pp elastic scattering at 100 and 300 GeV/c.

	100 GeV/c		300 GeV/c	
$-t$ (GeV^2)	$N(t)$	$\delta N(t)$	$N(t)$	$\delta N(t)$
0.18	361 779	1495	3.89×10^6	8.2×10^3
0.25	287 736	678	2.801×10^6	3.6×10^3
0.35	110 747	408	1.272×10^6	2.4×10^3
0.45	44 075	255	0.570×10^6	1.6×10^3
0.55	17 585	158	0.226×10^6	992
0.65	6 507	96	87.8×10^3	618
0.75	2 369	57	35 026	212
0.85	944	36	13 392	133
0.95	374	22	5 409	86
1.05	108	12.6	2 234	56.6
1.15	49.7	8.7	907	37.8
1.25	11.7	3.9	236	22.6
1.35	13.4	4.3	64	14.6
1.45	15.3	4.3	6.5	9.0
1.55			0	6.3
1.65			13.2	6.8
1.75			40.9	8.1
1.85			19.2	6.9
1.95			30.0	14.1

45 GeV/c exhibit quite a different structure: The polarization zero has moved in to smaller $|t|$ and instead of being positive near $t = -1$ GeV^2 the polarization parameter is zero or slightly negative. Since no data exist between 24 and 45 GeV/c, the details of how the polarization changes with momentum in this region remain unexplored. It is also worth noting that at 45 GeV/c the polarization

TABLE VIII. Polarization parameters for pp elastic scattering at 100 and 300 GeV/c.

	100 GeV/c			300 GeV/c	
$-t$ (GeV^2)	$P(t)$	$\delta P(t)$	$-t$ (GeV^2)	$P(t)$	$\delta P(t)$
0.15–0.20	0.0177	0.0055	0.150–0.175	0.0118	0.0083
0.20–0.25	0.0076	0.0047	0.175–0.200	0.0034	0.0053
0.25–0.30	0.0032	0.0055	0.200–0.225	0.0069	0.0052
0.30–0.35	–0.0179	0.0067	0.225–0.250	–0.0039	0.0056
0.35–0.40	–0.0225	0.0085	0.250–0.275	–0.0076	0.0064
0.40–0.45	–0.0006	0.0106	0.275–0.300	–0.0011	0.0073
0.45–0.50	–0.0213	0.0133	0.300–0.325	0.0113	0.0081
0.50–0.55	–0.0074	0.0172	0.325–0.350	0.0097	0.0084
0.55–0.60	–0.0265	0.0220	0.350–0.375	–0.0025	0.0089
0.60–0.65	–0.0295	0.0270	0.375–0.400	–0.0103	0.0097
0.65–0.70	–0.0485	0.0350	0.400–0.425	–0.0006	0.0114
0.70–0.80	0.0326	0.0357	0.425–0.450	–0.0276	0.0126
0.80–0.90	0.0295	0.0567	0.450–0.475	–0.0037	0.0142
0.90–1.00	–0.0357	0.0960	0.475–0.500	–0.0227	0.0158
1.00–1.10	–0.280	0.157	0.50 –0.55	–0.0046	0.0132
1.10–1.20	0.0098	0.2060	0.55 –0.60	–0.0136	0.0166
			0.60 –0.65	–0.0102	0.0094
			0.65 –0.70	–0.0162	0.0103
			0.70 –0.75	–0.0241	0.0123
			0.75 –0.80	–0.0176	0.0157
			0.80 –0.90	–0.0339	0.0156
			0.90 –1.00	–0.0488	0.0245
			1.00 –1.10	–0.0277	0.0368
			1.10 –1.20	–0.1110	0.0610
			1.20 –1.30	–0.152	0.096
			1.30 –1.40	–0.15	0.31
			1.60 –2.00	0.294	0.223

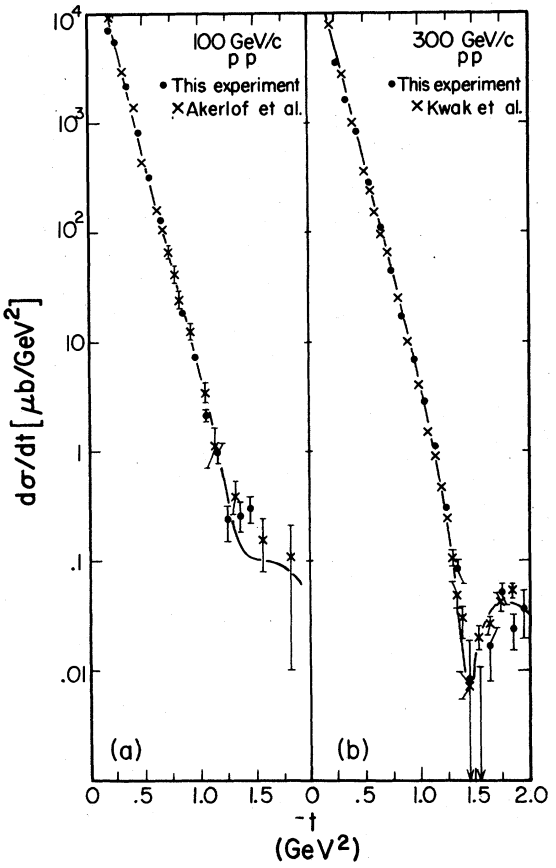

FIG. 15. Differential cross sections for pp elastic scattering at 100 and 300 GeV/c. The solid lines represent fits by the Kane and Seidl model.

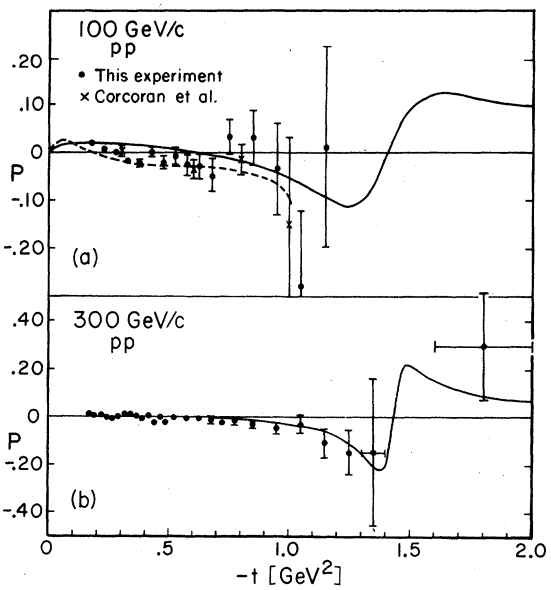

FIG. 16. Polarization parameters for pp elastic scattering at 100 and 300 GeV/c measured in this experiment, and at 110 GeV/c as determined by Corcoran *et al.* The solid lines represent predictions by the Kane and Seidl model, and the dashed line is a prediction by Irving (Ref. 6).

is only about 0.025 which is somewhat smaller than one might have predicted from a pole model with a single exchange-degenerate trajectory.

From our results, shown in Fig. 16, it can be seen that the polarization at small $|t|$ is still decreasing with increasing momentum. As in the Serpukhov data[15] the zero appears at smaller $|t|$ than it did in the data at lower momentum. Our results also show a trend to relatively large negative polarizations (~−0.05) with increasing $|t|$. There is no indication of a positive second lobe near $t = -1$ GeV^2, which is characteristic of the data below 20 GeV/c.

For model predictions we again turn to the absorption model of Kane and Seidl.[3] Since the model as published is in disagreement with a large body of new data which have been obtained since 1975, we have first reevaluated the parameters of this model by including the new data points in the fitting procedure. The resulting fits to the differential cross sections at 100 and 300 GeV/c and to the polarization parameters between 6 and 45 GeV/c are represented by the solid curves in Figs. 15 and 17, respectively. The only serious disagreement between the model fits and the data occurs with the polarization at 6 GeV/c, where the model gives a polarization parameter which is only about half as large as the measured one and which does not have any hint of the dip observed near $t = -0.9$ GeV^2. The dip and double-zero structure arise in the model from the fortuitous cancellation of amplitudes with quite different momentum dependence. Although the fit to the 6-GeV/c data can be improved by a different choice of the model parameters, the model would then fail to reproduce the polarization data at momenta greater than 10 GeV/c.

Using the same updated parameters, the Kane and Seidl model predicts that the pp polarization parameters at 100 and 300 GeV/c vary with t as shown by the solid curves in Fig. 16. In Fig. 18 the model prediction at 150 GeV/c is compared with the recent results obtained at the SPS.[20] The agreement between the model predictions and the polarization data above 45 GeV/c is good. For $|t| > 1$ GeV^2 our data at 300 GeV/c are suggestive of the structure predicted by the model, but unfortunately the statistical accuracy of our measurements in this t region is insufficient to place strong constraints on the model.

Finally, in Fig. 19 we show the polarization-parameter data which we obtained at 300 GeV/c without the spin-precession magnets in the inci-

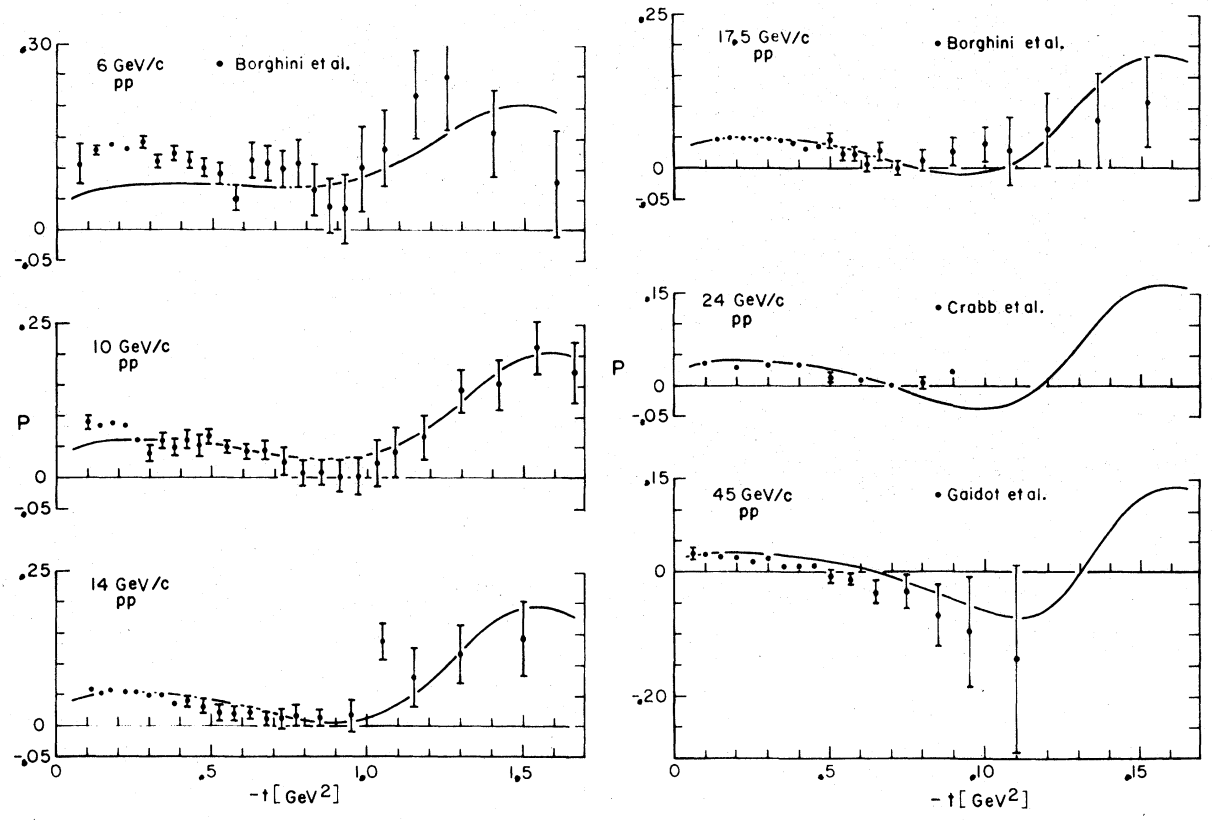

FIG. 17. Polarization parameters for *pp* elastic scattering between 6 and 45 GeV/*c*. The solid lines represent fits by the Kane and Seidl model.

dent beam. There is no statistically significant difference between these results and those of Fig. 16 which were obtained with the spin precession magnets. Both sets were taken with a 400 GeV primary proton beam striking the production target. The secondary beam line accepted particles which emerged at an average horizontal angle of 3.5 mrad. From this comparison we conclude that

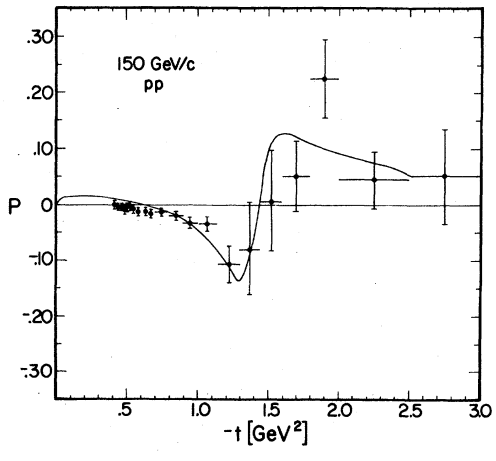

FIG. 18. Polarization parameters for *pp* elastic scattering at 150 GeV/*c* measured by Fidecaro *et al.* (Ref. 20). The solid line represents the prediction by the Kane and Seidl model.

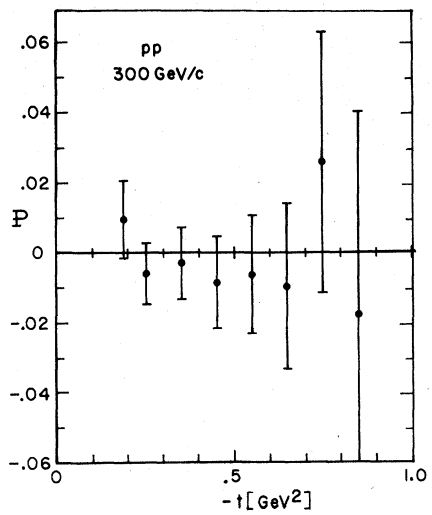

FIG. 19. Polarization parameters for *pp* elastic scattering at 300 GeV/*c* obtained without the spin precession magnets in the incident beam.

the polarization of the secondary proton beam was small or that the spin correlation parameter was small, or both.

Electromagnetic effects

Our results show that the polarizations observed in elastic $\pi^{\pm}p$ and pp scattering become quite small at high energies, due to the generally decreasing hadronic amplitudes. As a result, contributions from electromagnetic interactions may begin to produce noticeable effects on the observed polarizations, even at t values outside of the Coulomb-nuclear interference region. This has been pointed out by several authors.[21,22]

The size of the electromagnetically induced polarization in pp scattering has been calculated by Buttimore *et al.*[23] under the assumption that the hadronic polarization is zero: at an incident momentum of 100 GeV/c and for $|t| > 0.1$ GeV^2 it is $\lesssim 1\%$.

For pion-nucleon scattering Borie and Jakob[24] have made a numerical comparison between one-photon exchange amplitudes and isospin-odd hadronic amplitudes; even at incident momenta as low as 10 GeV/c they were comparable in magnitude for t values beyond the interference region. The magnitude of the electromagnetic effects is illustrated in Fig. 20, which shows the t dependence of the polarization difference

$$\Delta P = P(\pi^+p)\frac{d\sigma}{dt}(\pi^+p) - P(\pi^-p)\frac{d\sigma}{dt}(\pi^-p)$$

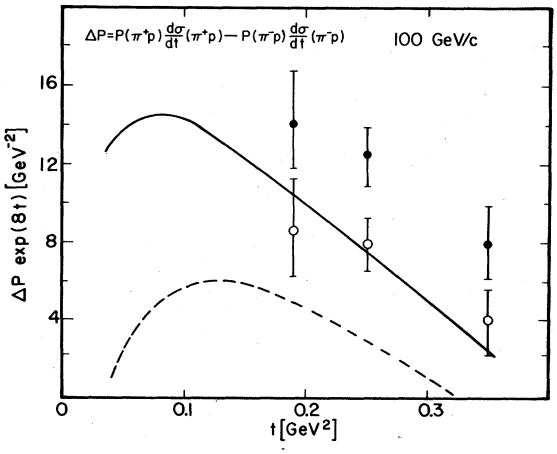

FIG. 20. t dependence of $\{P(\pi^+p)(d\sigma/dt)(\pi^+p) - P(\pi^-p)(d\sigma/dt)(\pi^-p)\}\exp(8t)$ at 100 GeV/c. The data points represent the results from this experiment before (solid points) and after (open points) subtraction of electromagnetic contributions. The solid curve is the prediction based on the pion-nucleon amplitudes of Ref. 26; applying the corrections for the electromagnetic contributions changes the solid curve to the dashed curve.

at 100 GeV/c (Ref. 25): the data points are calculated from the results of this experiment, both before and after correcting for the one-photon-exchange contribution; the curves represent predictions for ΔP based on the pion-nucleon scattering amplitudes extracted by Höhler *et al.*,[26] again before and after subtraction of electromagnetic effects. The corrections are comparable to or slightly larger than the experimental errors. Thus, it will be necessary to correct high-energy polarization data, including those presented in this paper, for electromagnetic effects before using them as input to detailed analyses of hadronic amplitudes.

ACKNOWLEDGMENTS

It is a pleasure to acknowledge R. Fuzesy's many and invaluable contributions to this experiment. We wish to thank E. Sadowski for his help with the design and construction of the Čerenkov counters, S. Dhawan, S. Olsen, and M. Urban for their substantial contributions to the PWC electronics, O. Fletcher and L. Ray for their assistance in installing and maintaining the polarized target, and D. Hornig for his work on the on-line programs. While the experiment enjoyed the cooperation of many members of the Fermilab staff, C. Brown, T. Droege, C. Kerns, Q. Kerns, T. Toohig, and the members of the Meson Laboratory and the Research Services Cryogenic Magnet Group deserve special mention. One of us (J.H.S.) wishes to thank A. Seidl for useful conversations on the implementation of the absorption model of Ref. 3. This work was supported in part by the U. S. Department of Energy.

APPENDIX

The following is a summary of the absorption model as described in the review article by Kane and Seidl[3] and in the references therein. The formulas required to implement the model are given and clarifications or corrections of the published model are noted.

The Kane and Seidl model is a strong absorption model without "nonsense wrong-signature zeros" in the residues. Apart from phase zeros all zeros in the amplitudes are the result of absorption. This is in contrast to the simple pole model and the absorption model of Fields and Stevens.[4] Thus, strong exchange degeneracy is not automatic in the Kane and Seidl model.

Amplitudes for the reaction $a+b \to c+d$ are generated as functions of s and t according to the usual Regge formulation with minor modifications:

$$R^{r}_{\lambda_c\lambda_d,\lambda_a\lambda_b}(s,t)=[\tfrac{1}{2}(-t)^{(n+x)/2}\gamma_{rca}(t)\gamma_{rdb}(t)]\left[\Gamma([J-\alpha_r(t)]/2)(s/s_0)^{\alpha_r(t)}\exp\left(-\frac{i\pi}{2}[\alpha_r(t)-J]\right)\right]. \quad \text{(A1)}$$

Here r denotes the Regge trajectory (ρ, f, ω, A_2, π, or B), J is the spin of the lowest mass physical particle on the trajectory, and γ_{rca} and γ_{rdb} are factorized pole residues; the subscripts λ_i are helicity indices, n is the net helicity flip, and x is the sum of the helicity flips at each vertex. The pole residues are parametrized as

$$\gamma_{rxy}=g_{rxy}\exp\{c_{rxy}[(\bar{m}^2-t)^{1/2}-\bar{m}]\}, \quad \text{(A2)}$$

with g the coupling constant at $t=0$, the s-channel helicity amplitude (SCHA) factor, and $\bar{m}$ the mass of the lowest t-channel threshold. The trajectory α_r is written as

$$\alpha_r(t)=J'+\frac{\alpha_{1r}(t-m_r^2)}{1+\alpha_{2r}/m_r^2-t}, \quad \text{(A3)}$$

where J' is the spin J of the lowest mass physical particle as before, plus any correction to the real part of the trajectory due to the dispersion integral over the width. The coefficients α_{1r} and α_{2r} are related to the $t=0$ slope and intercept of the trajectory,

$$\alpha_{1r}=[J-\alpha_r(0)]^2/\{2\alpha_r'(0)-[J-\alpha_r(0)]m_r^2\}, \quad \text{(A4a)}$$

$$\alpha_{2r}=2[J-\alpha_r(0)-\alpha_r'(0)m_r^2]/\{m_r[2\alpha_r'(0)m_r-J+\alpha_r(0)]\}. \quad \text{(A4b)}$$

The diffractive amplitude, the Pomeron in Regge language, is parametrized as

$$P(s,t)=-isR_c^2A_ce^{B_ct}J_1(R_c\sqrt{-t})/R_c\sqrt{-t}-isR_e^2A_ee^{B_et}J_0(R_e\sqrt{-t}), \quad \text{(A5)}$$

where

$$R_i^2=R_{i0}^2+R_{i1}^2\left(\ln(s)-\frac{i\pi}{2}\right). \quad \text{(A6)}$$

As is customary, the energy scale factor s_0 is taken to be 1 GeV^2. The linear dependence of the radii R_i^2 on $\ln(s)$ accounts for the shrinkage of the forward elastic peaks. The subscripts c and e refer to center and edge components, respectively.

Absorption has a natural geometrical interpretation in impact-parameter space; transformations between this space and t space are made via the Hankel transforms

$$R_{\gamma_c\gamma_d,\gamma_a\gamma_b}(s,b)=\frac{1}{2q^2}\int\sqrt{-t}d\sqrt{-t}R_{\lambda_c\lambda_d,\lambda_a\lambda_b}(s,t)J_n(b\sqrt{-t}), \quad \text{(A7a)}$$

$$R_{\gamma_c\gamma_d,\gamma_a\gamma_b}(s,t)=2q^2\int b\,db\,R_{\lambda_c\lambda_d,\lambda_a\lambda_b}(s,b)J_n(b\sqrt{-t}), \quad \text{(A7b)}$$

TABLE IX. Coupling constants for πN and NN scattering.

πN scattering Vertex	SCHA factor	Values
$\rho^0\pi^+\pi^-$	$\sqrt{2}g_{\rho^0\pi^+\pi^-}$	$g_{\rho^0\pi^+\pi^-}=6$
$f\pi^+\pi^-$	$\sqrt{2}g_{f\pi^+\pi^-}$	$g_{f\pi^+\pi^-}=6.9$
$\rho^0p(\frac{1}{2})\ p(\frac{1}{2})$	$\sqrt{2}G_V^\rho$	$G_V^\rho=1.65$
$\rho^0p(\frac{1}{2})\ p(-\frac{1}{2})$	$\sqrt{2}G_T^\rho/2m_N$	$G_T^\rho=20.7$
$fp(\frac{1}{2})\ p(\frac{1}{2})$	$\sqrt{2}G_V^f$	$G_V^f=26.9$
$fp(\frac{1}{2})\ p(-\frac{1}{2})$	$\sqrt{2}G_T^f/2m_N$	$G_T^f=4.24$
NN scattering Vertex	SCHA factor	Values
$\rho^0p(\frac{1}{2})\ p(\frac{1}{2})$	$\sqrt{2}G_V^\rho$	$G_V^\rho=4$
$\rho^0p(\frac{1}{2})\ p(-\frac{1}{2})$	$\sqrt{2}G_T^\rho/2m_N$	$G_T^\rho=7.9$

ω, A_2^0, f, π, and B couplings have the same forms as the ρ^0 couplings and numerical values:

$G_V^\omega=11$, $G_T^\omega=1.2$

$G_{V^2}^{A_2^0}=6.9$, $G_{T^2}^{A_2^0}=7.35$

$G_V^f=23.4$, $G_T^f=4.1$

$G_V^\pi=0$, $G_T^\pi=17.9$

$G_V^B=0$, $G_T^B=28$

with n the net helicity flip.

The elastic rescattering amplitude M (the absorption matrix) is defined as

$$M(s,t)=P(s,t)+K(2q/W)f(s,t)+\Sigma(s,t)\,, \qquad \text{(A8)}$$

with P the Pomeron, f the Regge f nonflip amplitude, and K an adjustable parameter ≈ 1. Σ is a parametrization of the contribution to absorption from the sum over all inelastic intermediate states,

$$\Sigma(s,t)=-isA_\Sigma e^{B_\Sigma t}(R_\Sigma{}^2+K_\Sigma)J_0(R_\Sigma\sqrt{-t})\,. \qquad \text{(A9)}$$

The absorption-corrected amplitudes are then

$$\tilde{R}_{\lambda_i}(s,b)=R_{\lambda_i}(s,b)\{1-i(2q^2/4\pi s)M(s,b)\} \qquad \text{(A10)}$$

and

$$\tilde{R}_{\lambda_i}(s,t)=2q^2\int b\,db\,\tilde{R}_{\lambda_i}(s,b)J_n(b\sqrt{-t})\,. \qquad \text{(A11)}$$

We note the following clarifications of, corrections to, and differences from the model described in the article by Kane and Seidl. First, our equations (A1), (A2), (A4), and (A8) are correct, while the corresponding equations in the review article contain typographical errors. Second, the diffractive amplitude in absorption is always transformed to impact-parameter space via a J_0, regardless of the helicity flip of the Regge amplitude which is to be absorbed, i.e.,

$$M(s,b)=\frac{1}{2q^2}\int\sqrt{-t}d\sqrt{-t}M(s,t)J_0(b\sqrt{-t})\,, \qquad \text{(A12)}$$

while $\tilde{R}_{\lambda_i}(s,t)$ is given by Eqs. (A10) and (A11). Third, it is not clear from the paper how the f contributes to Eq. (A8). A. Seidl has informed us that his prescription was to absorb the f via an approximate matrix

$$M_0(s,t)=P(s,t)+\Sigma(s,t)\,, \qquad \text{(A13)}$$

thereby defining an approximately absorbed f, denoted by f'. Then absorption of all amplitudes used in constructing observables is carried out with

$$M(s,t)=M_0(s,t)+K(2q/W)f'(s,t)\,. \qquad \text{(A14)}$$

Fourth, the article discusses in some detail the use of a helicity-flip "diffractive" amplitude. Again, Seidl has informed us that this term was not used in their fits nor have we found it necessary to include the term in ours. Fifth, the π and B trajectories, as parametrized in the article, have negative α_{2r} and consequently have poles at some value of negative t. We have replaced the trajectory parametrization (A3) for these two poles (but no others) by a linear trajectory[27]

TABLE X. Parameters determining Reggeon trajectories and residues for πN and NN scattering.

Parameter	Particle/vertex	πN	NN
s_0 (GeV^2)	all	1	1
$\alpha_r'(0)$ (GeV^{-2})	ρ^0	0.74[a]	0.83
	ω	1.1	1.1
	A_2^0	0.8	0.8
	f	0.8	0.8
	π	0.85	0.85
	B	0.55	0.55
$\alpha_r(0)$	ρ^0	0.45	0.47
	ω	0.25	0.25
	A_2^0	0.28	0.28
	f	0.4[a]	0.5
	π	−0.015	−0.015
	B	0.16	0.16
c_{rxy}	ρNN	1.365	1.365
	$\rho\pi\pi$	0.8	
	ωNN		1.92
	fNN	0.61	0.61
	$f\pi\pi$	0	
	A_2NN		0.47
	πNN		1.5
	BNN		1

[a]These values were suggested by A. Seidl (private communication).

TABLE XI. Parameters for Pomeron and absorption in πN and NN scattering.

Pomeron	πN[a]	NN
A_c	13.78	11.5
B_c	2.05	2.24
A_e	0.88	2
B_e	3.32	4.18
R_{c0}	2.23	2.19
R_{c1}	0.47	0.85
R_{e0}	0	0
R_{e1}	1.95	1.71
Inelastic intermediate states		
A_Σ	0.85	2.13
B_Σ	3.01	5.61
K_Σ	74.2	49.37
$R_{\Sigma 0}{}^2$	−3.49	0
$R_{\Sigma 1}{}^2$	5.51	10.02
K	0.889	0.889

[a]All of the πN parameters were suggested by A. Seidl (private communication).

$$\alpha(t) = \alpha(0) + \alpha'(0)t. \quad \text{(A15)}$$

Equations for calculating differential cross sections and polarization parameters for $\pi^{\pm}p$ and pp elastic scattering are given in Ref. 3. The updated parameters used in the calculations with the Kane and Seidl model as presented in this paper are listed in Tables IX, X, and XI.

---

*Present address: General Electric Company, Medical Systems Division, P. O. Box 414, Milwaukee, Wisc. 53201.
†Present address: CERN, Geneva, Switzerland.
‡Present address: Bell Telephone Laboratories, Holmdel, N.J. 07733.

[1]Two recent surveys of Regge-pole phenomenology are: P. D. B. Collins, *Regge Theory and High Energy Physics* (Cambridge University Press, Cambridge, England, 1977) and A. C. Irving and R. P. Worden, Phys. Rep. 34C, 117 (1977). Two older, but still useful surveys are: A. D. Martin and T. D. Spearman, *Elementary Particle Theory* (North-Holland, Amsterdam, 1970) and V. Barger and D. Cline, *Phenomenological Theories of High Energy Scattering* (Benjamin, New York, 1969).
[2]S. Chiu and A. W. Hendry, Phys. Rev. D 6, 190 (1972).
[3]G. Kane and A. Seidl, Rev. Mod. Phys. 48, 309 (1976).
[4]R. D. Field and P. R. Stevens, Caltech Report No. CALT-68-534, 1976 (unpublished).
[5]C. Bourrely *et al.*, J. Phys. G 3, 295 (1977).
[6]A. C. Irving, Nucl. Phys. B101, 263 (1975).
[7]C. W. Akerlof *et al.*, Phys. Rev. D 14, 2864 (1976).
[8]J. H. Snyder *et al.*, Phys. Rev. Lett. 41, 781 (1978); 41, 1256(E) (1978).
[9]I. P. Auer *et al.*, Phys. Rev. Lett. 39, 313 (1977).
[10]G. Bunce *et al.*, Phys. Rev. Lett. 36, 1113 (1976).
[11]D. Miller *et al.*, Phys. Rev. D 16, 2016 (1977).
[12]M. Borghini *et al.*, Phys. Lett. 31B, 405 (1970).
[13]M. Borghini *et al.*, Phys. Lett. 36B, 493 (1971).
[14]A. Gaidot *et al.*, Phys. Lett. 57B, 389 (1975).
[15]A. Gaidot *et al.*, Phys. Lett. 61B, 103 (1976).
[16]N. Kwak *et al.*, Phys. Lett. 58B, 233 (1975).
[17]M. D. Corcoran *et al.*, Phys. Rev. Lett. 40, 1113 (1978).
[18]M. Borghini *et al.*, Phys. Lett. 36B, 501 (1971).
[19]D. G. Crabb *et al.*, Nucl. Phys. B121, 231 (1977).
[20]M. Fidecaro, private communication, 1979; these results supercede those published in G. Fidecaro *et al.*, Phys. Lett. 76B, 369 (1978). We thank M. Fidecaro for making these results available to us prior to publication.
[21]A. P. Vanzha, L. I. Lapidus, and A. V. Tarasov, Yad. Fiz. 16, 1023 (1972) [Sov. J. Nucl. Phys. 16, 565 (1973)]; B. Z. Kopeliovich and L. I. Lapidus, Yad. Fiz. 19, 340 (1974) [Sov. J. Nucl. Phys. 19, 168 (1974)].
[22]C. Bourrely and J. Soffer, Lett. Nuovo Cimento 19, 569 (1977).
[23]N. H. Buttimore, E. Gotsman, and E. Leader, Phys. Rev. D 18, 694 (1978).
[24]E. Borie and H. P. Jakob, Phys. Lett. 78B, 323 (1978).
[25]This figure is the 100-GeV/c version of Fig. 1 in Ref. 24. We thank E. Borie for making it available to us.
[26]G. Höhler *et al.*, *Handbook of Pion-Nucleon Scattering* (ZAED, Eggenstein-Leopoldshafen, Germany, 1979).
[27]J. H. Snyder, Ph.D. thesis, Yale University, 1978 (unpublished).